NeuroImage 202 (2019) 116077

Contents lists available at ScienceDirect

NeuroImage

journal homepage: www.elsevier.com/locate/neuroimage

Quantitative MRI of cerebral white matter hyperintensities: A new approach towards understanding the underlying pathology

Elene Iordanishvili [a], Melissa Schall [a], Ricardo Loução [a], Markus Zimmermann [a], Ketevan Kotetishvili [b], N. Jon Shah [a,c,d,e], Ana-Maria Oros-Peusquens [a,*]

[a] Institute of Neuroscience and Medicine 4 (INM-4), Research Center Jülich, Jülich, Germany
[b] Department of Physics, Georgian Technical University, Tbilisi, Georgia
[c] Institute of Neuroscience and Medicine 11 (INM-11), Research Center Jülich, Jülich, Germany
[d] Jülich Aachen Research Alliance (JARA-BRAIN), Translational Medicine, Aachen, Germany
[e] Department of Neurology of the RWTH Aachen University, Aachen, Germany

ARTICLE INFO

Keywords:
Quantitative MRI
Deep white matter hyperintensities
Periventricular white matter hyperintensities
Fazekas scale

ABSTRACT

Interest in white matter hyperintensities (WMH), a radiological biomarker of small vessel disease, is continuously increasing. This is, in most part, due to our better understanding of their association with various clinical disorders, such as stroke and Alzheimer's disease, and the overlapping pathology of WMH with these afflictions. Although post-mortem histological studies have reported various underlying pathophysiological substrates, *in vivo* research has not been specific enough to fully corroborate these findings. Furthermore, post-mortem studies are not able to capture which pathological processes are the driving force of the WMH severity. The current study attempts to fill this gap by non-invasively investigating the influence of WMH on brain tissue using quantitative MRI (qMRI) measurements of the water content (H_2O), the longitudinal (T_1) and effective transverse relaxation times (T_2^*), as well as the semi-quantitative magnetization transfer ratio (MTR), and bound proton fraction (f_{bound}). In total, seventy subjects (age range 50–80 years) were selected from a population-based aging cohort study, 1000BRAINS. Normal appearing grey (NAGM) and white matter (NAWM), as well as deep (DWMH) and periventricular (PWMH) white matter hyperintensities, were segmented and characterized in terms of their quantitative properties. The subjects were then further divided into four grades according to the Fazekas rating scale of severity. Groupwise analyses of the qMRI values in each tissue class were performed. All five qMRI parameters showed significant differences between WMH and NAWM ($p < 0.001$). Importantly, the parameters differed between DWMH and PWMH, the latter having higher H_2O, T_1, T_2^* and lower MTR and f_{bound} values ($p < 0.001$). Following grading according to the Fazekas scale, DWMH showed an increase in the water content, T_1 and a decrease in bound proton fraction corresponding to severity, exhibiting significant changes in grade 3 ($p < 0.001$), while NAWM revealed significantly higher H_2O values in grade 3 compared to grade 0 ($p < 0.001$). PWMH demonstrated an increase in T_2^* values (significant in grade 3, $P < 0.001$). These results are in agreement with previous histopathological studies and support the interpretation that both edema and myelin loss due to a possible breakdown of the blood-brain barrier and inflammation are the major pathological substrates turning white matter into DWMH. Edema being an earlier contributing factor to the pathology, as expressed in the elevated water content values in NAWM with increasing severity. In the case of PWMH, an altered fluid dynamic and cerebrospinal fluid leakage exacerbate the changes. It was also found that the pathology, as monitored by qMRI, evolves faster in DWMH than in the PWMH following the severity.

Abbreviations: CSF, cerebrospinal fluid; DWMH, deep white matter hyperintensities; f_{bound}, bound proton fraction; FLAIR, fluid attenuated inversion recovery; meGRE, multi echo gradient recalled echo; MTR, magnetization transfer ratio; NAGM, normal appearing grey matter; NAWM, normal appearing white matter; PWMH, periventricular white matter hyperintensities; WMH, white matter hyperintensities.

* Corresponding author.
E-mail address: a.m.oros-peusquens@fz-juelich.de (A.-M. Oros-Peusquens).

https://doi.org/10.1016/j.neuroimage.2019.116077
Received 31 May 2019; Received in revised form 3 August 2019; Accepted 5 August 2019
Available online 6 August 2019

1. Introduction

Previously white matter hyperintensities (WMH) have been considered incidental and harmless findings in magnetic resonance imaging (MRI) associated with the aging process (Award et al., 1986; Prins and Scheltens, 2015). However, since being established as a radiological biomarker for small vessel disease (Hachinski et al., 1987; Wardlaw et al., 2015), WMH have become the target for numerous studies. Over the past two decades, increasing evidence as to the clinical importance of WMH has been accumulated, and several conditions, such as arterial stiffness (Singer et al., 2014) and hypertension, smoking, and high blood glucose level have been correlated with a higher occurrence of the pathology (Wardlaw et al., 2013a). WMH themselves increase the risk of stroke, cognitive decline, both vascular and Alzheimer's dementia, and even mortality rate (Debette and Markus, 2010). Furthermore, there is a known dose-dependent relationship between the severity of WMH and associated pathologies (Debette and Markus, 2010).

Several pathophysiological mechanisms have been proposed to contribute to the development of WMH and cause the heterogeneity of the underlying pathological substrate. The ischemic hypothesis explains white matter (WM) microstructural integrity loss due to hypoperfusion-hypoxic episodes, compromising the watershed regions (Rosenberg et al., 2016). Another potential mechanism is endothelial dysfunction and blood-brain barrier (BBB) disruption due to inflammatory processes, leading to fluid leakage and edema. Inflammation itself might be a part of the repair and remodeling process in the extracellular matrix after ischemia, causing the activation of microglia and astrocytes (Rosenberg, 2009). An alternative etiological factor for inflammation in small vessel disease is an infection via the brain-gut axis. Studies have shown a link between oral microbiotica, e.g., Streptococcus mutans and Porphyromans gingivalis, and an increased risk of cerebrovascular pathologies, including microbleeds and stroke. In addition, stroke itself can also lead to an altered microbiome and intestinal dysmotility via complex signaling pathways such as neuronal-glial-endothelial interactions or cytokines-induced activation of gut inflammatory and immune cells (Ihara and Yamamoto, 2016; Arya and Hu, 2018)."

Multiple visual scales have been proposed to assess the severity of WMH (for a summary see Griffanti et al., 2018), with the Fazekas scale being the most commonly used. The Fazekas scale starts from no WMH and ends with the most severe grade (Wahlund et al., 2001), and additionally divides the WMH into deep white matter hyperintensities (DWMH) and periventricular white matter hyperintensities (PWMH) (Fazekas et al., 1987). The need for this subdivision based on the spatial separation lies in the differences of the underlying pathology, as well as in functional relevance. For instance, PWMH have been mostly associated with cognitive impairment, while DWMH are linked more to mood disorders (Kim et al., 2008). Various post-mortem histological studies revealed axonal loss, myelin rarefaction, disruption of ependyma, and fluid accumulation as the pathological substrates for WMH (Pantoni and Simoni, 2003; Gouw et al., 2011). However, *in vivo* studies confirming these finding are scarce. Furthermore, post-mortem studies have mostly investigated severe WMH cases, and hence little is known in terms of which underlying mechanism is the driving force to increased severity. In contrast, the majority of imaging studies focus on evaluating the volume and the load of WMH using qualitative T_2-weighted fluid-attenuated inversion recovery (FLAIR) or T_1-weighted anatomical images in relation to severity and as a predictor of other disorders (DeCarli et al., 2005; Habes et al., 2016). Even though this research has improved our understanding of the pathophysiology and the clinical impact of WMH, tissue-specific *in vivo* microstructural changes still need to be elucidated.

Quantitative MRI (qMRI) is ideally suited for this task, as this method is not only able to provide site- and hardware-independent measures, thus allowing multi-center studies in large cohorts to take place, but also facilitates the measurement of parameters deeply related to tissue microstructure. These parameters include NMR relaxation times (Bottomley et al., 1984), especially when different water pools are characterized simultaneously (Mackay et al., 1984), water content (H_2O) (Tofts, 2003; Shah et al., 2011), and magnetization transfer (MT) parameters (Wolff and Balaban, 1989). Some of these quantities are known to be correlated (for example H_2O and R1 (Fatouros and Marmarou, 1999)), but they also show complementary information. Longitudinal T_1 and effective transverse T_2* relaxation times are tissue-specific biophysical parameters, simultaneously affected by several pathological processes such as edema, myelin or axonal loss, and inflammation (Tofts, 2003). The longitudinal relaxation time (or rate) is sensitive to the presence of macromolecules (Koenig, 1991; Rooney et al., 2007), and perhaps, additionally, to water content. In WM, the leading cause of T_1 relaxation was assigned to cholesterol in myelin (Koenig, 1991). T_2* is sensitive to the presence of susceptibility inhomogeneities in the tissue on a short distance scale, in addition to effects influencing T_2 and T_1 (Tofts, 2003). Unlike the relaxation times, water content mapping in brain tissue has a very direct biological interpretation (Tofts, 2003) as it describes the percentage of mobile water in the voxel. These are the protons with relaxation times (>2 ms) long enough to be detected with standard clinical MRI equipment ($TE \geq 2$ ms). The complement percentage of the voxel is taken by protons with very short relaxation times, which are not directly detectable and elements other than proton and water oxygen. Water content is tightly regulated in healthy subjects and is affected by mechanisms creating brain edema or inflammation (Shah et al., 2011). MT parameters (MTR, f_{bound}) reflect the magnetization or chemical exchange between the free and macromolecular proton pools and are sensitive to alterations in the macromolecular content, in particular to changes in myelin (Tozer et al., 2005). Despite the low specificity to a single mechanism of each qMRI parameter, a combination of these quantities has the potential to expand our understanding of the WMH pathology.

In this study, the aforementioned quantitative parameters were used, for the first time, to unravel the underlying pathology and relationship with severity behind the WMH, non-invasively. The objective of the study was two-fold. First, we compared DWMH with PWMH to see if they exhibit differences in qMRI parameters and thus, presumably, a distinctive pathological substrate reflecting differences in tissue microstructure. Additionally, we compared DWMH and PWMH to normal appearing white matter (NAWM) in order to investigate the magnitude of the changes. Second, we explored the evolution of the disease in DWMH, PWMH, and NAWM separately, as a function of the qMRI parameters' alteration in the relationship with the severity of white matter lesions. Cortical thinning has already been reported in WMH (Wardlaw et al., 2015), revealing that the pathology also affects normal appearing grey matter (NAGM). Therefore, we also looked at qMRI changes in NAGM.

2. Materials and methods

2.1. Subjects

A sub-cohort of seventy subjects (age range 50–80 years, mean = 70 years) was drawn from the 1000BRAINS project database, an epidemiological and neuroscientific study of an elderly German cohort with data gathered from extensive MR imaging (Caspers et al., 2014). Prior to the study, written informed consent was given by all participants. The study protocol was approved by the Duisburg-Essen University ethics committee in accordance with the Declaration of Helsinki (Caspers et al., 2014). Participants underwent extended computer-assisted interviews related to their lifestyle, disease and medication history in addition to laboratory work and psychological tests (Caspers et al., 2014). One hundred and eighty-seven subjects underwent a full qMRI protocol and FLAIR sequence and were selected for this study. The scans were checked for the data quality and for the incidental findings by an experienced MRI scientist and by a radiologist. Images with movement artifacts, wrong field of view or incidental pathological findings seen on FLAIR were excluded. From the remaining dataset, participants with a history of any other diseases affecting the central nervous system (CNS), such as

epilepsy or depression were excluded. The other exclusion criteria consisted of CNS affecting medication intake such as pshycholeptics or pshychoanaleptics. Additionally, only non-demented individuals, as assessed by a dementia-detection (DemTect) test (score>7), were included. DemTect is a psychometric screening tool assessing working memory, verbal memory, verbal fluency performance and intellectual flexibility (total score 18). It evaluates age adequate cognitive performance (13–18 points) and is sensitive to mild cognitive impairment (9–12 point) and early dementia (≤8) (Kalbe et al., 2004). The WMH load (total lesion volume and total lesion number) of the remaining seventy subjects was checked by a radiologist (E.I.). Subsequently, the subjects were divided into four groups according to severity following the Fazekas scale starting from grade 0 (no WMH) to grade 3 (confluent irregular WMH larger than 20 mm). Table 1 summarizes the characteristics of the sub-cohort for each group of Fazekas grading.

2.2. MRI data acquisition and pre-processing

All subjects underwent MR measurements on a 3 T scanner (Tim-TRIO, Siemens Medical Systems, Erlangen, Germany) from 2016 until January 2018. A body coil was used for excitation and a 32-channel phased-array coil was used for signal reception. The qMRI protocol was based on four 3D multi-echo gradient echo (meGRE) sequences, with and without MT preparation (off-resonance frequency −1,5 kHz), complemented by an actual flip angle imaging sequence (AFI) (Yarnykh, 2007) to map the transmit field. Additionally, a T_2-weighted FLAIR sequence was used to evaluate the WMH. Sequence acquisition parameters can be seen in Table 2.

The quantitative T_1, T_2* and H_2O maps were derived according to the 3D two-point method described in (Schall et al., 2018). MT parameters, namely the magnetization transfer ratio (MTR) and bound proton fraction (f_{bound}) were calculated as follows (Tofts, 2003):

$$MTR = \frac{M_0 - M_0(MT)}{M_0} * 100\ (\%);\ f_{bound} = \frac{MTR}{T_1},$$

where M_0 is the longitudinal magnetization without MT preparation, M_0(MT) is the corresponding magnetization with MT preparation. and T_1 is the longitudinal relaxation time of the free water pool (no MT preparation).

We point out that MTR calculated in this manner describes the fractional reduction of longitudinal magnetization created by the MT pulses. It is similar to the quantity delta (∂) introduced by Helms et al. (2008), with the difference that we describe the effect of the whole MT preparation on the steady state.

Table 1
Characteristics of the study cohort.

Characteristics	Grade 0	Grade 1	Grade 2	Grade 3
Age, years	64 (9)	67 (7)	71 (4)	74 (6)
Gender n, female/male	5/12	13/11	8/7	4/10
Waist circumference, cm	91 (10)	91 (11)	93 (13)	98 (13)
Systolic blood pressure, mmHg	124 (13)	119 (13)	125 (17)	132 (15)
Diastolic blood pressure, mmHg	76 (9)	73 (9)	76 (10)	78 (8)
High blood pressure [antihypertensives]	11 [0]	12 [3]	6 [1]	10 [3]
Stage 0.5	9	10	4	7
Stage 1	2	2	2	3
Stage 2	0	0	1	0
Glycated Haemoglobin, %	5.6 (0.3)	5.8 (0.7)	5.8 (0.3)	6 (0.4)
Total cholesterol, mg/dl	216 (37)	214 (28)	242 (39)	220 (35)
Low-density lipoprotein, mg/dl	135 (27)	129 (25)	140 (31)	131 (33)
High-density lipoprotein, mg/dl	61 (12)	65 (13)	71 (20)	65 (15)
Triglycerides, mg/dl	116 (50)	94 (60)	138 (79)	120 (40)
High sensitivity C-reactive protein, mg/l	0.19 (0.24)	0.25 (0.38)	0.17 (0.2)	0.44 (0.59)
Dementia-detection test	14 (2)	16 (2)	15 (2)	14 (2)

Values are depicted mean (standard deviation), except gender, where number of female/male is given. High blood pressure stages are given according to the seventh report of the joint national committee on prevention, detection, evaluation, and treatment of high blood pressure (JNC-7). The number of people with hypertension taking antihypertensive medication is given in [].

2.3. WMH segmentation

T_2-weighted FLAIR images of each subject were transformed to the space of the quantitative maps using the Statistical Parametric Mapping (SPM 12, https://www.fil.ion.ucl.ac.uk/spm/) software package (Collignon et al., 1995). Thereafter, WMH segmentation was carried out automatically using the Lesion Segmentation Tool (LST), which is an SPM12 toolbox. This toolbox requires T_2-weighted FLAIR images as input and utilizes a lesion prediction algorithm for segmentation (Schmidt et al., 2012).

To avoid the misclassification of the lesions, the segmented WMH masks were visually checked and modified, where necessary, by a radiologist following the guidelines set out in the standards for reporting vascular changes on neuroimaging (STRIVE) (Wardlaw et al., 2013b). Furthermore, WMH were divided into two groups: DWMH and PWMH. In grades 1 and 2, the separation was carried out visually, while in grade 3, as the lesions are already confluent, a distance of 10 mm from the lateral ventricles was used for the separation (Griffanti et al., 2018). To avoid partial volume effects, voxels that were at least 95% likely to belong to CSF, were excluded from the PWMH mask. This was achieved using the CSF probability mask described below. Fig. 1 shows the DWMH and PWMH masks on the FLAIR and on the concomitant quantitative maps.

The volume of the WMH, DWMH and PWMH were calculated separately using the respective segmentation mask. This was done by multiplying the number of voxels and the voxel size given in milliliters.

2.4. MRI data post-processing

The first echo of the T_1-weighted meGRE sequence of each subject was used to derive tissue probability maps for grey (GM) and white matter as well as CSF using the unified segmentation algorithm in SPM12 (Ashburner and Friston, 2005). Only voxels with a probability of at least 97% of belonging to WM or GM were included in the corresponding binary tissue masks. Finally, all the voxels belonging to the segmented WMH masks were excluded from the WM and GM, resulting in NAWM and NAGM masks.

2.5. Statistical analyses

The mean values of the lesion volume and its range for WMH, DWMH and PWMH were calculated over all subjects and separately in each grade of the Fazekas scale.

The mean values and the standard deviations of all MR parameters: T_1, T_2*, water content, MTR and f_{bound} in the NAWM, NAGM, DWMH, and PWMH were calculated for each subject. Groupwise mean values and standard deviations for each grade of the Fazekas scale were also measured. Thereafter, outliers for each tissue class, divided according to severity, were calculated using the 1.5 interquartile rule and were excluded from the further statistical analyses (Tukey, 1977).

To investigate the first objective of the study, a one-way analysis of variance (ANOVA), or in the case of non-parametric data, a Kruskal-Wallis test was used. The qMRI parameters were presented as continuous variables. We checked whether they were significantly different among the four tissue classes: NAWM, DWMH, PWMH and NAGM. The data were further divided into four groups according to the Fazekas scale and the same objective was investigated in each grade separately.

An analysis of covariance (ANCOVA) was used to assess changes in the qMRI parameters of each tissue class according to severity, hence evaluating the second objective of this study. qMRI values in each tissue class were presented as continuous dependent variables and the Fazekas scale was used as a categorical independent variable. High blood pressure

Table 2
MRI sequence acquisition parameters.

Imaging parameters	M_0 - weighted meGRE (MT)	T_1 - weighted meGRE (MT)	Actual Flip Angle sequence	T_2 - weighted FLAIR
Repetition time	50 ms	50 ms	150 ms	9 s
Flip angle	7°	40°	40°	150°
First echo time, [ΔTE]	2.19 [2.55] ms	2.19 [2.55] ms	3.7 ms	100 ms
Number of echoes	18 (12)	18 (12)	1	1
Resolution	$1 \times 1 \times 2\,mm^3$	$1 \times 1 \times 2\,mm^3$	$2.8 \times 2.8 \times 4\,mm^3$	$0.9 \times 0.9 \times 4\,mm^3$

meGRE = multi echo gradient echo; MT = magnetization transfer; FLAIR = fluid attenuated inversion recovery; ΔTE = delta echo time; ms = millisecond; mm = millimeter.

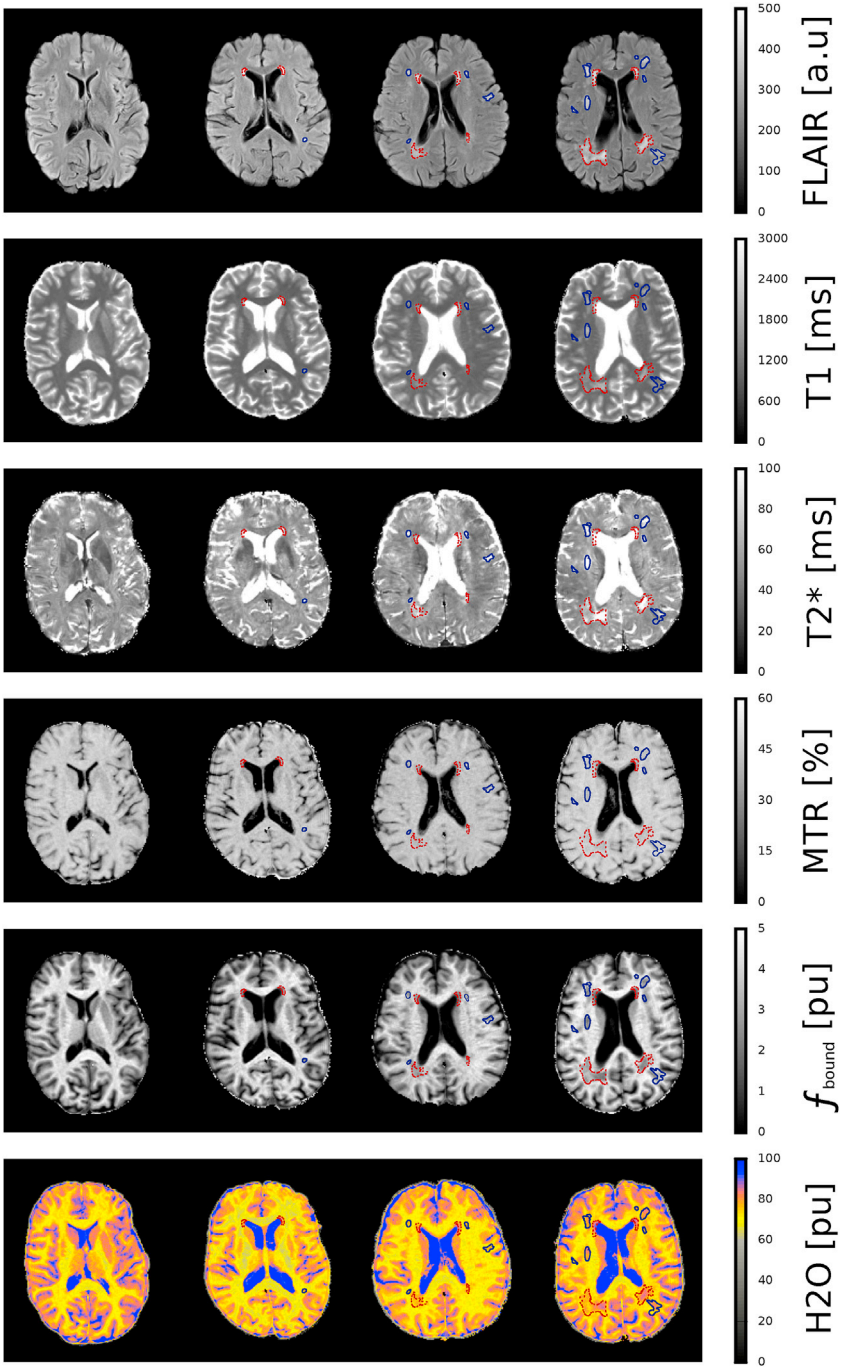

Fig. 1. An exemplary segmentation of deep (blue solid) and periventricular (red dotted) white matter hyperintensities. Segmented masks are shown on FLAIR and on concomitant quantitative maps in all grades of the Fazekas scale.

values were characterized in 4 stages according to the seventh report of the Joint National Committee on Prevention, Detection, Evaluation, and Treatment of High Blood Pressure (JNC-7) (Report, 2003). These stages, as well as age, were included as covariates, as older age and hypertension are known to be the major risk factors for developing WMH (Jeerakathil et al., 2004). Additionally, to check whether antihypertensive medication intake in the hypertensive subjects affected the qMRI values, an independent sample *t*-test with multiple comparison correction was conducted between the participants on these medications and drug-naive participants, while controlling for high blood pressure values. The homogeneous distribution of the covariates across all levels of the independent variable was validated using ANOVA. The eta squared (η^2) was calculated to assess the effect size for both ANOVA and ANCOVA, and omega squared (ω^2) was calculated for Welch's test. Additionally, the effect size was evaluated for each covariate separately in ANCOVA. If $\eta^2 < 0.001$ for any of the covariates, we considered that the contribution of this particular covariate was too small to explain the variance in the dependent variable and excluded it from the final analysis. Cramer's V was used for the effect size calculation in the case of the non-parametric Kruskal-Wallis test.

Before applying ANOVA or ANCOVA, the underlying assumptions for both tests were verified. The Shapiro-Wilk test was used to check the normal distribution of all parameters in each tissue class before and after separating in the four grades of the Fazekas scale. The homogeneity of variance was assessed using the Levene's test. Tukey's range test was used for a pairwise multiple comparison correction for both ANOVA and ANCOVA in the case of Levene's test being non-significant. If the homogeneity of variance assumption was not met, Welch's test with the Games-Howell for multiple comparison correction was applied. The Games-Howell test is similar to the Tukey range test, but it uses Welch's degree of freedom and is thus reliable even in the case of unequal variance and sample size (Lee and Dong, 2018). For ANCOVA, a linear regression model was additionally used to check the homogeneity of the regression slopes between the covariates and the independent variable. In the case of non-parametric data, a Dwass-Steel-Critchlow-Fligner pairwise comparison was performed after the Kruskal-Wallis test. The Dwass-Steel-Critchlow-Fligner test is based on the Wilcoxon rank sum calculation and provides family-wise error rate protection (Crichtlow and Fligner, 1991). The significance level for the whole statistical analysis was set to $p < 0.001$.

The entire statistical analysis was carried out in the open source spreadsheet Jamovi (version 0.9.1.12, https://www.jamovi.org/), based on the R statistical language (www.r-project.org), and SPSS software (version 23, IBM, Chicago, USA).

2.6. Data availability

Anonymized data, supporting the study findings, are available upon reasonable request via the corresponding author.

3. Results

Fig. 2 shows the volume and the range of the lesions in each grade of the Fazekas scale and, in addition, the total range in WMH, DWMH and PWMH. The values increase according to the severity.

Table 3 shows the groupwise mean values and the standard deviations of all quantitative parameters for NAWM, NAGM, DWMH and PWMH in each grade of the Fazekas scale for seventy subjects. While

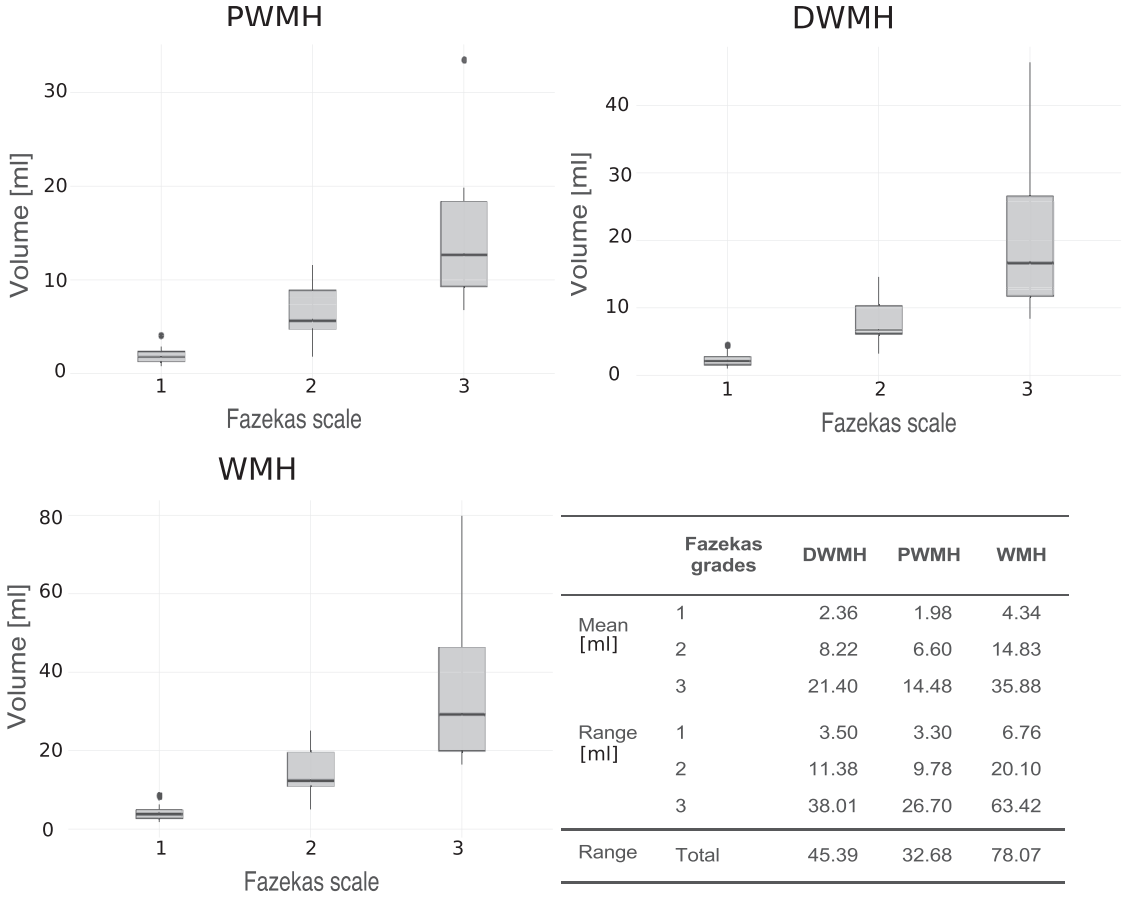

	Fazekas grades	DWMH	PWMH	WMH
Mean [ml]	1	2.36	1.98	4.34
	2	8.22	6.60	14.83
	3	21.40	14.48	35.88
Range [ml]	1	3.50	3.30	6.76
	2	11.38	9.78	20.10
	3	38.01	26.70	63.42
Range	Total	45.39	32.68	78.07

Fig. 2. Volume and range of WMH lesions in each grade of the Fazekas scale. The boxplots depict the distribution of the WMH, DWMH and PWMH volumes. The black line indicates the median and the black dots represent the outliers. The mean values of the lesion volume and the range are also provided in the table.

Table 3
Mean values and the standard deviations of the quantitative MRI parameters in all tissue classes divided according to severity.

Tissue classes	Fazekas scale	H_2O, p.u	T_1, ms	T_2*, ms	MTR, %	f_{bound}, p.u.
NAWM	Grade 0	71.1 ± 1.4	1052 ± 52	52 ± 2.0	45.4 ± 1.0	4.4 ± 0.3
	Grade 1	71.0 ± 1.4	1067 ± 38	53 ± 2.6	45.0 ± 1.2	4.3 ± 0.2
	Grade 2	71.7 ± 1.9	1095 ± 49	52 ± 2.9	45.1 ± 1.4	4.2 ± 0.3
	Grade 3	73.5 ± 1.4	1131 ± 59	55 ± 3.0	44.9 ± 1.5	4.0 ± 0.4
DWMH	Grade 1	74.1 ± 1.8	1219 ± 94	68 ± 9.8	43.4 ± 1.3	3.6 ± 0.3
	Grade 2	75.1 ± 2.1	1274 ± 78	68 ± 6.3	43.4 ± 1.5	3.5 ± 0.3
	Grade 3	76.9 ± 1.8	1336 ± 86	73 ± 5.5	43.5 ± 2.1	3.4 ± 0.3
PWMH	Grade 1	77.7 ± 1.8	1435 ± 119	69 ± 6.9	40.2 ± 1.7	3.0 ± 0.3
	Grade 2	77.9 ± 2.1	1445 ± 79	75 ± 7.8	41.2 ± 2.0	3.0 ± 0.2
	Grade 3	79.1 ± 1.8	1515 ± 91	81 ± 7.0	41.6 ± 2.1	2.9 ± 0.3
NAGM	Grade 0	81.1 ± 1.3	1630 ± 53	58 ± 2.1	40.2 ± 1.3	2.6 ± 0.1
	Grade 1	81.1 ± 1.3	1634 ± 36	57 ± 2.5	40.2 ± 1.2	2.5 ± 0.3
	Grade 2	81.5 ± 1.6	1672 ± 59	57 ± 1.9	40.0 ± 1.7	2.4 ± 0.2
	Grade 3	82.8 ± 1.4	1695 ± 46	58 ± 2.5	39.8 ± 1.5	2.4 ± 0.1

NAWM = normal appearing white matter; DWMH = deep white matter hyperintensities; PWMH = periventricular white matter hyperintensities; NAGM = normal appearing grey matter; MTR = magnetization transfer ratio; p.u = percentage units; ms = millisecond.

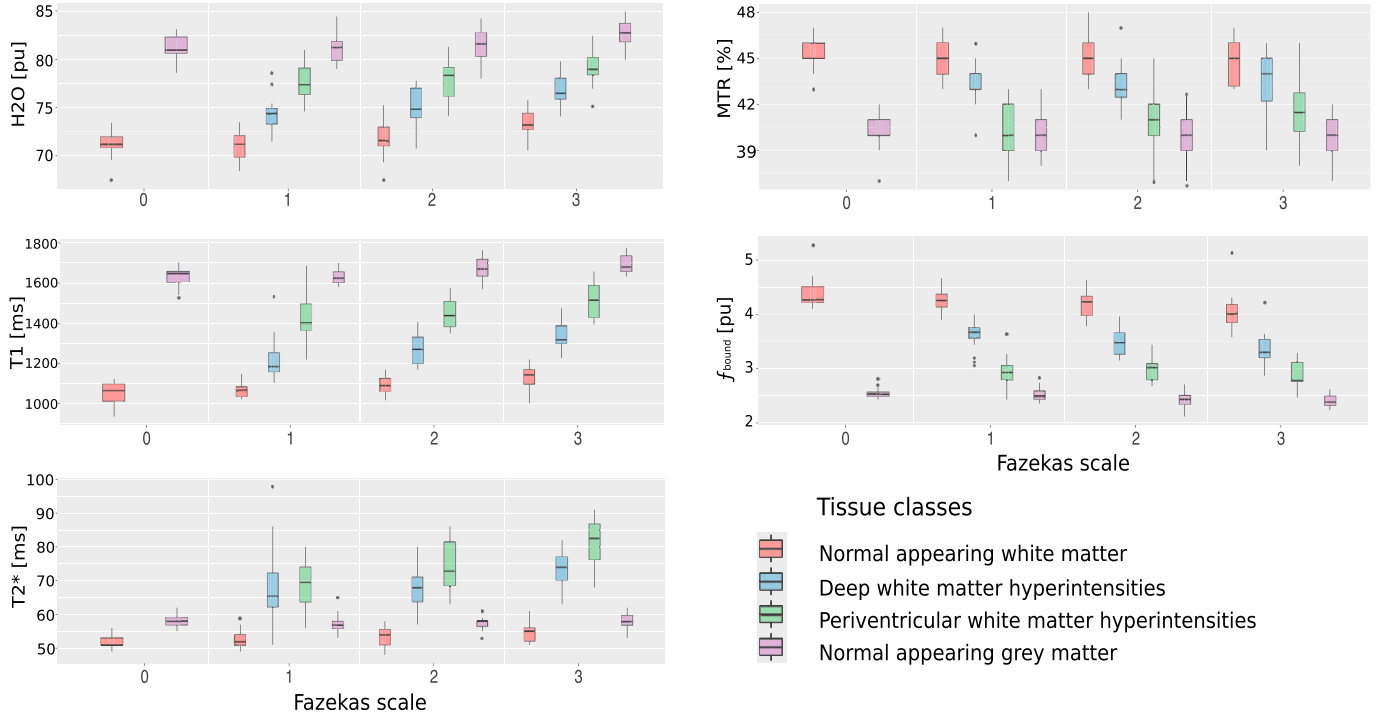

Fig. 3. Quantitative MRI parameter distribution of each tissue class according to the Fazekas scale. Boxes reflect the median and interquartile range. Whiskers depict 5th and 95th percentiles. The black dots show outliers. NAWM = normal appearing white matter (red); DWMH = deep white matter hyperintensities (blue); PWMH = periventricular white matter hyperintensities (green); NAGM = normal appearing grey matter (purple).

Fig. 3 depicts the data distribution accordingly. The mean values of all qMRI parameters for each subject, including outliers depicted in red, are summarized in Supplementary Table 1.

The H_2O, T_1, MTR, and f_{bound} values were normally distributed in each tissue classes. T_2* showed non-Gaussian distributions for ANOVA. However, when divided according to the Fazekas scale, all the measured MRI data demonstrated a normal distribution, except for the T_1 values of the tissue classes in grade 1 for ANOVA. The homogeneity of variance was violated in all parameters, except H_2O, when analyzed without the Fazekas scale. After separation according to severity, only T_1 (grade 1) and T_2* (grade 1, 2, 3) had heterogeneous variances. High blood pressure values according to JNC-7 were homogeneously distributed across all levels of the independent variable (Fazekas scale). An independent sample *t*-test showed no statistically significant difference between the qMRI values of the participants on antihypertensive medication and the drug-naive participants, except for T_2* in NAWM. In this case, antihypertensive medication intake was also considered as a covariate in ANCOVA. Age showed heterogeneous distribution between grade 0 and 3. The linear regression between the covariates and the independent variable showed homogeneous slopes.

The quantitative parameters exhibited significant differences between WMH and NAWM ($p < 0.001$). In comparison to NAWM, lesions were characterized by an increased H_2O, T_1, T_2* and decreased MTR and f_{bound} (Fig. 4a-e; boxplots). Additionally, all qMRI parameters were able to differentiate between NAGM and the lesions ($p < 0.001$), with the exception of MTR between PWMH and NAGM ($p = 0.027$) (Fig. 4 e; boxplots). When divided into the four grades of the Fazekas scale according to severity, the trend of the qMRI parameters was the same, except for the MTR (grades 2 and 3), which did not exhibit statistically significant differences between NAWM and DWMH (Fig. 4 e) ($p = 0.003$ for grade 2 and $p = 0.177$ for grade 3). Table 4 shows the effect size for ANOVA according to severity, as well as p values for all tissue classes.

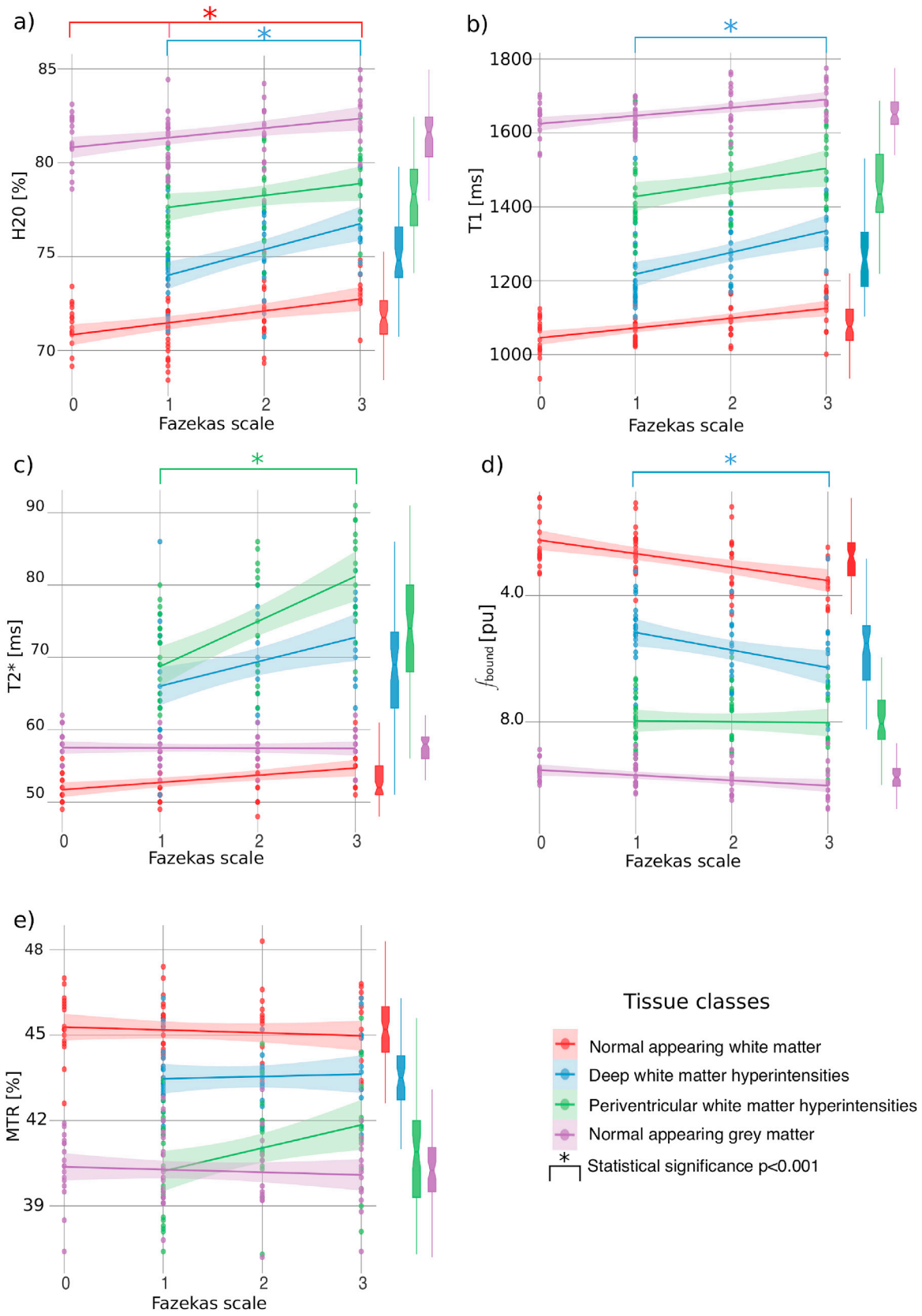

Fig. 4. The changes of quantitative MRI parameters following the Fazekas scale of severity in each tissue class. The regression line with the standard error is fitted for every tissue separately. The boxplots represent normal appearing white-, grey matter, deep and periventricular white matter hyperintensities overall without division according to severity. The dots represent the data points.

Table 4
P-values of ANOVA checking the significant difference of the qMRI parameters among tissue classes in each grade of Fazekas scale. η^2, ω^2, Cramer's V - effect size.

Grade 0 Tissue classes	p-value	Tissue classes	Grade 1 Tissue classes	p-value	Tissue classes	Grade 2 Tissue classes	p-value	Tissue classes	Grade 3 Tissue classes	p-value	Tissue classes
a) H_2O: p-values of ANOVA among tissue classes in each grade of the Fazekas scale											
NAWM	<0.001	NAGM	NAWM	<0.001	DWMH	NAWM	<0.001	DWMH	NAWM	<0.001	DWMH
				<0.001	PWMH		<0.001	PWMH		<0.001	PWMH
				<0.001	NAGM		<0.001	NAGM		<0.001	NAGM
			DWMH	<0.001	PWMH	DWMH	<0.001	PWMH	DWMH	<0.001	PWMH
				<0.001	NAGM		<0.001	NAGM		<0.001	NAGM
			PWMH	<0.001	NAGM	PWMH	<0.001	NAGM	PWMH	<0.001	NAGM
$\eta^2 = 0.944$			$\eta^2 = 0.876$			$\eta^2 = 0.783$			$\eta^2 = 0.847$		
b) T_1: p-values of ANOVA among tissue classes in each grade of the Fazekas scale.											
NAWM	<0.001	NAGM	NAWM	<0.001	DWMH	NAWM	<0.001	DWMH	NAWM	<0.001	DWMH
				<0.001	PWMH		<0.001	PWMH		<0.001	PWMH
				<0.001	NAGM		<0.001	NAGM		<0.001	NAGM
			DWMH	<0.001	PWMH	DWMH	<0.001	PWMH	DWMH	<0.001	PWMH
				<0.001	NAGM		<0.001	NAGM		<0.001	NAGM
			PWMH	<0.001	NAGM	PWMH	<0.001	NAGM	PWMH	<0.001	NAGM
$\eta^2 = 0.974$			Cramer's V = 0.54			$\eta^2 = 0.915$			$\eta^2 = 0.899$		
c) T_2*: p-values of ANOVA among tissue classes in each grade of the Fazekas scale.											
NAWM	<0.001	NAGM	NAWM	<0.001	DWMH	NAWM	<0.001	DWMH	NAWM	<0.001	DWMH
				<0.001	PWMH		<0.001	PWMH		<0.001	PWMH
				<0.001	NAGM		<0.001	NAGM		0.054	NAGM
			DWMH	0.65	PWMH	DWMH	0.095	PWMH	DWMH	0.012	PWMH
				<0.001	NAGM		<0.001	NAGM		<0.001	NAGM
			PWMH	<0.001	NAGM	PWMH	<0.001	NAGM	PWMH	<0.001	NAGM
$\eta^2 = 0.722$			$\omega^2 = 0.613$			$\omega^2 = 0.715$			$\omega^2 = 0.831$		
d) MTR: p-values of ANOVA among tissue classes in each grade of the Fazekas scale.											
NAWM	<0.001	NAGM	NAWM	<0.001	DWMH	NAWM	0.003	DWMH	NAWM	0.177	DWMH
				<0.001	PWMH		<0.001	PWMH		<0.001	PWMH
				<0.001	NAGM		<0.001	NAGM		<0.001	NAGM
			DWMH	<0.001	PWMH	DWMH	0.013	PWMH	DWMH	0.044	PWMH
				<0.001	NAGM		<0.001	NAGM		<0.001	NAGM
			PWMH	0.995	NAGM	PWMH	0.036	NAGM	PWMH	0.040	NAGM
$\eta^2 = 0.886$			η^2 0.745			$\eta^2 = 0.668$			$\eta^2 = 0.552$		
e) f_{bound}: p-values of ANOVA among tissue classes in each grade of the Fazekas scale.											
NAWM	<0.001	NAGM	NAWM	<0.001	DWMH	NAWM	<0.001	DWMH	NAWM	<0.001	DWMH
				<0.001	PWMH		<0.001	PWMH		<0.001	PWMH
				<0.001	NAGM		<0.001	NAGM		<0.001	NAGM
			DWMH	<0.001	PWMH	DWMH	<0.001	PWMH	DWMH	<0.001	PWMH
				<0.001	NAGM		<0.001	NAGM		<0.001	NAGM
			PWMH	<0.001	NAGM	PWMH	<0.001	NAGM	PWMH	<0.001	NAGM
$\omega^2 = 0.974$			η^2 - 0.947			$\eta^2 = 0.899$			$\eta^2 = 0.883$		

The statistical analysis yielded significant differences between DWMH and PWMH. In general, higher T_1, T_2* and H_2O values were found in PWMH compared to the deep counterparts, while MTR and f_{bound} showed the opposite behavior. All the parameters reached statistical significance, except for T_2* ($p = 0.004$). The same trend in the qMRI parameters appeared after dividing the lesions according to severity. H_2O, T_1 and f_{bound} of DWMH and PWMH were significantly different from each other in every grade ($p < 0.001$). T_2* did not show any significant changes. MTR values didn't exhibit a statistically significant difference between DWMH and PWMH in grade 2($p = 0.013$) and 3($p = 0.044$).

In order to further evaluate the evolution of the disease and its influence on WM and GM, as well as on the lesions, we analyzed the behavior of the qMRI properties for each tissue class following the Fazekas scale. For this purpose, a general linear model, adjusted for age and blood pressure values, was used. Fig. 4 depicts the linear changes of the qMRI parameters in the NAWM and NAGM, as well as in the WMH according to severity following the Fazekas scale. A positive trend, mostly in NAWM and WMH, is noticeable in T_1, T_2* and the water content, while f_{bound} shows a negative trend in these tissues. T_1, H_2O, and the bound proton fraction of DWMH between the grades 1–3, and the T_2* of PWMH between grades 1–3 reached statistical significance. The same was true for the H_2O values of NAWM between grades 1–3 and 0–3. NAGM showed a non-systematic behavior in all measured parameters and none of them reflected significant changes. There was also no significant alteration of the MTR parameter in any of the tissue classes. Table 5 shows the p-values of the ANCOVA among the Fazekas grades and the effect sizes in all tissue classes separately.

4. Discussion

In this qMRI study, we investigated non-demented subjects with WMH, using the high levels of sensitivity afforded by qMRI. First, brain tissue was divided into four classes: DWMH, PWMH, NAWM and NAGM. The qMRI properties of each class were analyzed separately. The results revealed significantly different qMRI values between DWMH and PWMH.

Table 5
P-values of ANCOVA checking the significant changes in all 5 qMRI parameters for each tissue class according to the severity using Fazekas scale. η^2, ω^2, Cramer's V - effect size.

NAWM			DWMH			PWMH			NAGM		
Fazekas grades	p-value	Fazekas grades	Fazekas grades	p-value	Fazekas grades	Fazekas grades	p-value	Fazekas grades	Fazekas grades	p-value	Fazekas grades
a) H_2O: p-values of ANCOVA across the Fazekas grades in each tissue class separately.											
0	0.855	1							0	0.999	1
	0.543	2								0.618	2
	<0.001	3								0.006	3
1	0.115	2	1	0.046	2	1	0.964	2	1	0.575	2
	<0.001	3		<0.001	3		0.066	3		0.002	3
2	0.024	3	2	0.014	3	2	0.116	3	2	0.082	3
$\eta^2 = 0.316$			$\eta^2 = 0.359$			$\eta^2 = 0.111$			$\eta^2 = 0.188$		
b) T_1: p-values of ANCOVA across the Fazekas grades in each tissue class separately.											
0	0.977	1							0	0.936	1
	0.522	2								0.643	2
	0.023	3								0.167	3
1	0.661	2	1	0.049	2	1	0.985	2	1	0.235	2
	0.023	3		<0.001	3		0.301	3		0.025	3
2	0.290	3	2	0.099	3	2	0.244	3	2	0.707	3
$\eta^2 = 0.127$			$\eta^2 = 0.285$			$\eta^2 = 0.269$			$\eta^2 = 139$		
c) T_2^*: p-values of ANCOVA across the Fazekas grades in each tissue class separately.											
0	0.941	1							0	0.008	1
	0.950	2								0.115	2
	0.256	3								0.241	3
1	0.676	2	1	0.442	2	1	0.132	2	1	0.962	2
	0.056	3		0.005	3		<0.001	3		0.832	3
2	0.458	3	2	0.079	3	2	0.054	3	2	0.986	3
$\eta^2 = 0.077$			$\eta^2 = 0.188$			$\eta^2 = 0.269$			$\eta^2 = 0.139$		
d) MTR: p-values of ANCOVA across the Fazekas grades in each tissue class separately.											
0	0.729	1							0	0.860	1
	0.708	2								0.498	2
	0.406	3								0.191	3
1	0.997	2	1	0.765	2	1	0.344	2	1	0.828	2
	0.840	3		0.941	3		0.263	3		0.398	3
2	0.930	3	2	0.946	3	2	0.971	3	2	0.902	3
$\eta^2 = 0.035$			$\eta^2 = 0.01$			$\eta^2 = 0.053$			$\eta^2 = 0.066$		
e) f_{bound}: p-values of ANCOVA across the Fazekas grades in each tissue class separately.											
0	0.927	1							0	0.998	1
	0.345	2								0.319	2
	0.004	3								0.224	3
1	0.561	2	1	0.004	2	1	0.618	2	1	0.290	2
	0.005	3		<0.001	3		0.984	3		0.189	3
2	0.122	3	2	0.102	3	2	0.554	3	2	0.987	3
$\eta^2 = 0.184$			$\eta^2 = 0.362$			$\eta^2 = 0.027$			$\eta^2 = 0.093$		

Second, we demonstrated altered qMRI parameters in WMH compared to NAWM. Third, the subjects were further divided into four groups using the Fazekas visual rating scale of severity, and from this we were able to show that the severity of the disorder influenced the qMRI parameters of the WMH and the NAWM.

We found DWMH and PWMH to be distinguishable from each other, based on the significantly different quantitative parameters between them, suggesting distinct underlying pathological substrates most probably reflecting divergent microstructural properties. In particular, PWMH showed increased T_1, T_2*, H_2O values and decreased MTR and f_{bound} values, as compared to DWMH. Water content, as measured here, largely reflects the voxel percentage of mobile water in tissue and has, therefore, a direct biological meaning. At the very least, an increase in MR-measured H_2O values significantly above the tightly regulated normal levels can be used as an objective definition of edema. Water content is increased in the interstitial edema found in WMH (Shah et al., 2011; Wardlaw et al., 2015), which is imaged by its FLAIR hyperintensity (Rojas and Eisenberg, 2012).

FLAIR used here with clinical parameters (Echo time (TE) = 100 ms, Inversion time (TI) = 2500 ms) is very sensitive to prolonged T_2 due to its long TE (White et al., 1992). Increased water content also contributes to the contrast via the equilibrium magnetization (Mulkern et al., 1990; White et al., 1992). But the contrast between the lesions and a tissue seen on water content maps is much less pronounced than that of FLAIR. We can use the T_2* values reported here as a surrogate for T_2. In lesions both T_2* and H_2O are increased. Since T_2 of free water, such as CSF, is at least an order of magnitude longer than that of water in tissue, even a small 'free water' compartment contributes to lengthening the resulting T_2

substantially.

In addition, FLAIR has a long TI, which ensures nulling of the long T_1 signal from CSF (Mulkern et al., 1990; White et al., 1992). It can therefore enhance contrast between regions with different T_1 values (Saranathan et al., 2017). Since increase in water content is usually correlated with increase in T_1 values (Fatouros and Marmarou, 1999), this offers an additional mechanism of enhanced visualization of WMH. Furthermore, the inversion pulse also perturbs the equilibrium between the free water and bound proton pools, thus creating another source of contrast between lesions and NAWM (Gochberg and Gore, 2007). This is moreover enhanced by the substantial MT effects offered by the 180^0 refocusing pulses in a 2D sequence (Turner et al., 2008). Consequently, FLAIR integrates the changes in several quantitative parameters between WMH and NAWM, as identified here, in a very synergistic way to create the striking contrast which led to the name 'hyperintensities'.

Both DWMH and PWMH showed altered qMRI parameters compared to NAWM. An increased H_2O indicates edema in WMH, with PWMH being more edematous compared to DWMH. T_1 and T_2* complement this finding as they are also influenced by the presence of edema (Tofts, 2003). Additionally, Myelin cholesterol and especially its hydroxyl (-OH) group is the main mechanism driving the T_1 contrast between WM and GM (Koenig et al., 1991), making this parameter sensitive to demyelination. T_1 has also been shown to reflect microglial activation, which is an indicator of inflammation, as well as myelin and axonal loss in post-mortem WMH reinforced by immunohistochemical staining (Gouw et al., 2008).

MTR and f_{bound} are known to be more specific to myelin alteration, with the later parameter, in particular, having a slightly higher sensitivity to myelin loss (Tofts, 2003). The trend in MTR in our study appears less sensitive to the evolution of pathology than that of the most other quantitative parameters. In fact, MTR in both DWMH and PWMH didn't show any change according to the severity. Additionally, there was no statistically significant difference in MTR values of DWMH and NAWM in grade 2 and 3. Here we define MTR as being the quantitative effect of the MT preparation pulses on reducing the equilibrium longitudinal magnetization due to magnetization exchange, similar to Helms et al. (2008). In addition to reflecting the macromolecular content of a tissue and magnetization exchange rates, it is expected to be influenced by possible direct saturation of the free water pool, by the longitudinal relaxation, and by the properties of the RF pulse used in the MT preparation (Henkelman et al., 2001). Off-resonance frequency, pulse power and repetition time of the pulsed irradiation, all contribute to creating the measured effect. Whereas there is a lack of consensus in deriving MTR in the clinic, and it is a largely sequence-parameter-specific measure, we would like to point out that most MTR values in the literature include a higher degree of T_1-weighting (Henkelman et al., 2001; Helms et al., 2008). Furthermore, the effect of the MT preparation on the equilibrium magnetization reflects the relative contribution of two mechanisms: magnetization transfer (reducing longitudinal magnetization) and longitudinal relaxation (leading to recovery of longitudinal magnetization) (Henkelman et al., 2001). Longer T_1 values, as seen in the lesions and increasing with higher grades of the Fazekas scale, would be associated with higher MTR values if the properties of the macromolecular pool remained the same. However, the bound proton fraction is decreasing, leading to a decrease in the effect of MT. These opposite effects contribute to reducing the variation of MTR with the severity, and thus make it a poor indicator of evolution of the disease. This, however, does not appear to be an exception. In an experimental animal model of autoimmune encephalomyelitis, f_{bound} was already found to be reduced in the WM lesions where MTR values were in a normal range (Rausch et al., 2009). In addition to a reduced sensitivity of MTR, as defined here, to the pathology, the changes in NAWM can contribute to mask to some extent the changes in the WMH. Altered H_2O and f_{bound} values in NAWM point towards the pathological changes. Although not significantly, MTR values in NAWM decrease according to the severity and get close to the same parameter values in DWMH.

Our results also show that DWMH are more prone to alterations corresponding with severity, as compared to PWMH. This is shown by a significantly higher rate of change in H_2O, T_1, and f_{bound} values between grades 3 and 1, compared to PWMH. The same temporal evolution of pathological substrates has been proposed in the literature due to disruption of the BBB leading to an altered interstitial fluid movement (Taheri et al., 2011; Wardlaw et al., 2015). Interestingly, NAWM also exhibited changes along the Fazekas scale, which is reflected in the significantly higher water content values in grade 3 compared to grades 0 and 1. Additionally, the fact that f_{bound} demonstrated decreasing values according to the severity, almost reaching the significant difference between grade 3 and grades 0 ($p = 0.004$) and 1 ($p = 0.005$), indicate that an increasing H_2O might be the driving pathological force behind the increase in WMH severity happening earlier than myelin loss.

Few studies have investigated the relationship between the MR appearance of WMH and histopathological findings (Prins and Scheltens, 2015). Even fewer have studied the qMRI properties of these lesions *in vivo* in order to disentangle the various underlying pathological substrates and confirm the histology (Wardlaw et al., 2015). Early research on post-mortem specimens of WMH and their concomitant MRI investigation revealed myelin rarefaction and gliosis caused by ischemic damage in the DWMH regardless of their severity, while PWMH additionally demonstrated edema due to altered periventricular fluid dynamics and CSF leakage (Fazekas et al., 1993). Although the lesions were clearly visible on FLAIR images, they were not distinguishable from each other. Our study complements these findings *in vivo*. Increased water content, T_1 and T_2* values in WMH compared to NAWM point out to the presence of brain edema, gliosis and demyelination. Additionally, lower MTR and f_{bound} values of the lesions, which are more specific to the myelin loss, support the histology. Furthermore, the fact that we were able to show higher water content values in the PWMH compared to the DWMH is in agreement with the altered periventricular fluid movement theory. Periventricular venous collagenosis causes decreased drainage of the fluid via the veins and the discontinuation of periventricular ependymal lining leads to edema (Fazekas et al., 1993; Brown et al., 2002). Another explanation for the changed qMRI parameters might be the altered brain clearance. The glymphatic system – a glial-dependent pathway – regulates the waste product clearance from the interstitial space via aquaporin-4 water channels. It also maintains balance between the CSF and the interstitial fluid (ISF) (Benveniste et al., 2019). Impaired ISF drainage and expansion of the extracellular space due to fluid accumulation has been shown to play a role in WMH development (Weller et al., 2015).

Quantitative T_1 mapping has been used previously in a small number of reports for the study of WMHs in post-mortem brains (Gouw et al., 2008) and *in vivo* (Aradi et al., 2013; Anderson et al., 2014). Gouw et al., have demonstrated increased T_1 values of WMH compared to NAWM both in Alzheimer's disease and non-demented elderly post-mortem brains. Higher T_1 values in WMH of migraine patients have been reported *in vivo* (Aradi et al., 2013). Anderson et al. have demonstrated the trend $T_1(NAWM) < T_1(DWMH) < T_1(PWMH)$ on 7 T (Anderson et al., 2014). Our results were found to be consistent with these reports in terms of changes in T_1 between WMHs and NAWM, as well as between DWMH and PWMH. In addition, we have directly investigated the quantitative water content changes in WMHs *in vivo*, without relying on correlation to T_1 values and have recorded the influence of the disease severity on the quantitative parameters.

Changes in the water content and bound proton fraction in the DWMH corresponding to severity, as evidenced by our study, suggests that demyelination, plays a major role in the evolution of WMH. The fact that the qMRI values of NAWM demonstrate the same trend as those of DWMH with the severity of the affliction, suggests the continuum nature of the pathology and these changes can be referred to as the "dirty-appearing white matter (DAWM)". This term has been used for describing the alterations in NAWM of multiple sclerosis patients not visible with conventional MRI (Ge et al., 2003), which coincide with

myelin loss in the immunohistochemical analysis and depicts a changing trend of the qMRI parameters similar to those found in our study (Moore and Laule, 2012).

Our study has some limitations. First, the cohort only contains cross-sectional data. As the WMH load is a function of time, it is desirable to investigate the progression of the pathology longitudinally. Second, the small number of subjects in each group of the Fazekas scale limits the statistical power. Third, due to acquisition resolution difference between 2D FLAIR with thick axial slices and 3D quantitative images co-registration was performed, which might introduce some partial volume effects and make the WMH mask less reliable at the axial boundaries. That is to say, as the FLAIR images were transformed to the quantitative imaging space, it might have an influence on the lesion segmentation, especially in the first grade of the Fazekas scale, when WMH are quite small and scattered. Fourth, age is not homogeneously distributed across the Fazekas grades 1 and 3. Although the data were age corrected, this may have influenced the ANCOVA results between grades 1 and 3. Finally, future studies with a bigger sample size and a more stratified cohort are needed to validate and expand our knowledge about the qMRI findings in sporadic, as well as in genetically caused WMH, such as those occurring in the cerebral autosomal dominant arteriopathy with subcortical infarcts and leukoencephalopathy (CADASIL).

To conclude, our *in vivo* study expands on the previous research and corroborates histological findings of WMH. Our data are able to differentiate between PWMH and DWMH with more specificity, and additionally, to the best of our knowledge, it is the first study to investigate the extent of the pathology and to observe the changes in qMRI parameters according to the severity of the disease.

Funding

Prof. Dr. N. J. Shah was funded partly by the Helmholtz Alliance ICEMED, Imaging and Curing Environmental Metabolic Diseases (HA-314), through the Initiative and Network Fund of the Helmholtz Association. As the Helmholtz Alliance contributes to the institutional funding, the grant does not imply any conflict of interest for this particular study.

Conflicts of interest

Authors report no conflict of interest.

Acknowledgments

We thank the investigative group and the staff of the 1000BRAINS study, especially Dr. Svenja Caspers, Dr. Susan Moebus, Nora Bittner and Dr. Noreen Pundt.

Appendix A. Supplementary data

Supplementary data to this article can be found online at https://doi.org/10.1016/j.neuroimage.2019.116077.

References

Anderson, V.C., Obayashi, J.T., Kaye, J.A., Quinn, J.F., Berryhill, P., Riccelli, L.P., Rooney, W.D., 2014. Longitudinal relaxographic imaging of white matter hyperintensities in the elderly. Fluids Barriers CNS 11 (1), 1–10. http://doi.org/10.1186/2045-8118-11-24.

Aradi, M., Schwarcz, A., Perlaki, G., Orsi, G., Kovács, N., Trauninger, A., Pfund, Z., 2013. Quantitative MRI studies of chronic brain white matter hyperintensities in migraine patients. Headache 53 (5), 752–763. http://doi.org/10.1111/head.12013.

Arya, AwadheshK., Hu, Bingren, 2018. "Brain–Gut Axis after stroke. Brain Circ. 4 (4), 165. http://doi.org/10.4103/bc.bc_32_18.

Ashburner, J., Friston, K.J., 2005. Unified segmentation. Neuroimage 26, 839851. http://doi.org/10.1016/j.neuroimage.2005.02.018.

Benveniste, H., Liu, X., Koundal, S., Sanggaard, S., Lee, H., Wardlaw, J., 2019. The glymphatic system and waste clearance with brain Aging : a review, 2nd ed. Gerontology 65, 106–119. https://doi.org/10.1159/000490349.

Bottomley, P.A., Foster, T.H., Argersinger, R.E., Pfeifer, L.M., 1984. A review of normal tissue hydrogen NMR relaxation times and relaxation mechanisms from 1 – 100 MHz : dependence on tissue type, NMR frequency, temperature, species, excision, and age, 11. Med Phys., pp. 425–448. http://doi.org/10.1118/1.595535

Brown, W.R., Moody, D.M., Challa, V.R., Thore, C.R., Anstrom, J.A., 2002. Venous collagenosis and arteriolar tortuosity in leukoaraiosis. J. Neurol. Sci. 15 (203–204), 159–163. http://doi.org/10.1016/S0022-510X(02)00283-6.

Caspers, S., Moebus, S., Lux, S., Pundt, N., Schütz, H., Mühleisen, T.W., Amunts, K., 2014. Studying variability in human brain aging in a population-based German cohort-rationale and design of 1000BRAINS. Front. Aging Neurosci. 6 (JUL), 1–14. http://doi.org/10.3389/fnagi.2014.00149.

Collignon, A., Maes, F., Delaere, D., Vandermeulen, D., Suetens, P., Marchal, G., 1995. Automated multi-modality image registration based on information theory. In: 14th International Conference on Information Processing in Medical Imaging, pp. 263–274. http://doi.org/10.1007/11784012_16.

Crichtlow, D.E., Fligner, M.A., 1991. On distribution-free multiple comparisons in the one-way analysis of variance. Commun. Stat. Theor. Methods 20 (1), 127. https://doi.org/10.1080/03610929108830487.

Debette, S., Markus, H.S., 2010. The clinical importance of white matter hyperintensities on brain magnetic resonance imaging: systematic review and meta-analysis. BMJ 341 (jul26 1) c3666–c3666. http://doi.org/10.1136/bmj.c3666.

DeCarli, C., Fletcher, E., Ramey, V., Harvey, D., Jagust, W.J., 2005. Anatomical mapping of white matter hyperintensities (WMH): exploring the relationships between periventricular WMH, deep WMH, and total WMH burden. Stroke 36 (1), 50–55. http://doi.org/10.1161/01.STR.0000150668.58689.f2.

Fatouros, P.P., Marmarou, A., 1999. In vivo measurements of brain water in humans using magnetic resonance imaging: method and normal values. J. Neurosurg. 90, 109–115. https://doi.org/10.3171/jns.1999.90.1.0109.

Fazekas, F., Chawluk, J.B., Alavi, A., Hurtig, H.I., Zimmerman, R.A., 1987. Mr signal abnormalities at 1.5-T in Alzheimer dementia and normal aging. Am. J. Roentgenol. 149 (2), 351–356. http://doi.org/10.2214/ajr.149.2.351.

Fazekas, F., Kleinert, R., Offenbacher, H., Schmidt, R., Kleinert, G., Payer, F., Lechner, H., 1993. Pathologic correlates of incidental MRI white matter signal hyperintensities. Neurology 43 (9), 1683–1689. http://doi.org/10.1212/WNL.43.9.1683.

Ge, Y., Grossman, R.I., Babb, J.S., He, J., Mannon, L.J., 2003. Dirty-Appearing White Matter in Multiple Sclerosis : Volumetric MR Imaging and Magnetization Transfer Ratio Histogram Analysis, 10th, ed. AJNR Am J Neuroradiol. 24, 1935–1940 December.

Gochberg, D.F., Gore, J.C., 2007. Quantitative magnetization transfer imaging via repetition times, 2nd ed. Magn Reson Med. 57, 437–441. https://doi.org/10.1002/mrm.21143.

Gouw, A.A., Seewann, A., van der Flier, W.M., Barkhof, F., Rozemuller, A.M., Scheltens, P., Geurts, J.J.G., 2011. Heterogeneity of small vessel disease: a systematic review of MRI and histopathology correlations. J. Neurol. Neurosurg. Psychiatry 82 (2), 126–135. http://doi.org/10.1136/jnnp.2009.204685.

Gouw, A.A., Seewann, A., Vrenken, H., Van Der Flier, W.M., Rozemuller, J.M., Barkhof, F., Scheltens, P., Geurts, J.J.G., 2008. Heterogeneity of white matter hyperintensities in Alzheimer's disease: post-mortem quantitative MRI and neuropathology. Brain 131 (12), 3286–3298. http://doi.org/10.1093/brain/awn265.

Griffanti, L., Jenkinson, M., Suri, S., Zsoldos, E., Mahmood, A., Filippini, N., Sexton, C.E., Topiwala, A., Allan, C., Kivimäki, M., Singh-Manoux, A., Ebmeier, K.P., Mackay, C.E., Zamboni, G., 2018. Classification and characterization of periventricular and deep white matter hyperintensities on MRI: a study in older adults. Neuroimage 15 (170), 174–181. http://doi.org/10.1016/j.neuroimage.2017.03.024.

Habes, M., Erus, G., Toledo, J.B., Zhang, T., Bryan, N., Launer, L.J., Davatzikos, C., 2016. White matter hyperintensities and imaging patterns of brain ageing in the general population. Brain 139 (4), 1164–1179. http://doi.org/10.1093/brain/aww008.

Hachinski, V.C., Potter, P., Merskey, H., 1987. In: Leuko-Araiosis, 1st ed., vol. 44, pp. 21–23 Arch Neurol.

Helms, G., Dathe, H., Kallenberg, K., Dechent, P., 2008. High-resolution maps of magnetization transfer with inherent correction for RF inhomogeneity and T1 relaxation obtained from 3D flash MRI. Magn. Reson. Med. 60, 1396–1407. https://doi.org/10.1002/mrm.21732.

Henkelman, R.M., Stanisz, G.J., Graham, J.S., 2001. Magnetization transfer in MRI: a review. NMR Biomed. 14, 57–64. https://doi.org/10.1002/nbm.683.

Ihara, M., Yamamoto, Y., 2016. Emerging evidence for pathogenesis of sporadic cerebral small vessel disease. Stroke 47 (2), 554–560. http://doi.org/10.1161/STROKEAHA.115.009627.

Jeerakathil, T., Wolf, P.A., Beiser, A., Massaro, J., Seshadri, S., D'Agostino, R.B., DeCarli, C., 2004. Stroke risk profile predicts white matter hyperintensity volume: the Framingham study. Stroke 35, 1857–1861. http://doi.org/10.1161/01.STR.0000135226.53499.85.

Kalbe, E., Kessler, J., Calabrese, P., Smith, R., Passmore, A.P., Brand, M., Bullock, R., 2004. DemTect: a new, sensitive cognitive screening test to support the diagnosis of mild cognitive impairment and early dementia. Int. J. Geriatr. Psychiatry 19 (2), 136–143. http://doi.org/10.1002/gps.1042.

Kim, K.W., Macfall, J.R., Payne, M.E., 2008. Classification of whitte matter lesions on magnetic resonance imaging in the elderly. Biol. Psychiatry 64 (4), 273–280. http://doi.org/10.1016/j.biopsych.2008.03.024.Classification.

Koenig, S.H., 1991. Cholesterol of myelin is the determinant of gray-white contrast in MRI of brain. Magn. Reson. Med. 20, 285–291. https://doi.org/10.1002/mrm.1910200210.

Lee, Sangseok, Lee, Dong Kyu, 2018. What is the proper way to apply the multiple comparison test? Korean J. Anesthesiol. 71 (5), 353–360. https://doi.org/10.4097/kja.d.18.00242.

Mackay, A., Whittall, K., Adler, J., Li, D., Paty, D., Graeb, D., 1984. In vivo visualization of myelin water in brain by magnetic resonance. Magn. Reson. Med. 673–677, 2011–2011. https://doi.org/10.1002/mrm.1910310614.

Moore, G.R.W., Laule, C., 2012. Neuropathologic correlates of magnetic resonance imaging in multiple sclerosis. J. Neuropathol. Exp. Neurol. 71 (9), 762–778. http://doi.org/10.1097/NEN.0b013e3182676388.

Mulkern, R.V., Wong, S.T.S., Winalski, C., Jolesz, F.A., 1990. Contrast manipulation and artifact assessment of 2D- and 3D-RARE sequences. Magn. Reson. Imag. 8, 557. https://doi.org/10.1016/0730-725X(90)90132-L.

Pantoni, L., Simoni, M., 2003. Pathophysiology of cerebral small vessels in vascular cognitive impairment, 1, 59–65.

Prins, N.D., Scheltens, P., 2015. White matter hyperintensities, cognitive impairment and dementia: an update. Nat. Rev. Neurol. 11 (3), 157–165. http://doi.org/10.1038/nrneurol.2015.10.

Rausch, M., Tofts, P.S., Levrik, P., Walmsley, A.R., Mir, A., Schubart, A., Seabrook, T., 2009. Characterization of white matter damage in animal models of multiple sclerosis by magnetization transfer ratio and quantitative mapping of the Apparent bound proton fraction F*. Mult. Scler. 15 (1), 16–27. https://doi.org/10.1177/1352458508096006.

Report, T.S., 2003. Prevention, detection, evaluation, and treatment of. Blood Press. 289 (19), 1206–1252. http://doi.org/10.1161/01.HYP.0000107251.49515.c2.

Rojas, R., Eisenberg, R.L., 2012. Cerebral edema, pp. 258–274 (September). https://doi.org/10.2214/AJR.11.8081.

Rooney, W.D., Johnson, G., Li, X., Cohen, E.R., Kim, S.-G., Ugurbil, K., Springer Jr., C.S., 2007. Magnetic field and tissue dependencies of human brain longitudinal 1H2O relaxation in vivo. Magn. Reson. Med. 57, 308–318. https://doi.org/10.1002/mrm.21122.

Rosenberg, G.A., 2009. Inflammation and white matter damage in vascular cognitive impairment. Stroke 40 (3 Suppl. 1), 20–23. http://doi.org/10.1161/STROKEAHA.108.533133.

Rosenberg, G.A., Wallin, A., Wardlaw, J.M., Markus, H.S., Montaner, J., Wolfson, L., Hachinski, V., 2016. Consensus statement for diagnosis of subcortical small vessel disease. J. Cereb. Blood Flow Metab. 36 (1), 6–25. http://doi.org/10.1038/jcbfm.2015.172.

Saranathan, M., Worters, P.W., Rettmann, D.W., Winegar, B., Becker, J., 2017. Physics for Clinicians : fluid-attenuated inversion recovery (FLAIR) and double inversion recovery (DIR). Imaging 1–11. https://doi.org/10.1002/jmri.25737.

Schall, M., Zimmermann, M., Iordanishvili, E., Gu, Y., Jon Shah, N., Oros-Peusquens, A.-M., 2018. A 3D two-point method for whole-brain water content and relaxation time mapping: comparison with gold standard methods. PLoS One 13 (8). http://doi.org/10.1371/journal.pone.0201013.

Schmidt, P., Gaser, C., Arsic, M., Buck, D., Förschler, A., Berthele, A., Mühlau, M., 2012. An automated tool for detection of FLAIR-hyperintense white-matter lesions in Multiple Sclerosis. Neuroimage 59 (4), 3774–3783. http://doi.org/10.1016/j.neuroimage.2011.11.032.

Shah, N.J., Ermer, V., Oros-Preusquens, A.M., 2011. Measuring the absolute water content of the brain using quantitative MRI. Methods Mol. Biol. 711, 29–64. https://doi.org/10.1007/978-1-61737-992-5_3.

Singer, J., Trollor, J.N., Baune, B.T., Sachdev, P.S., Smith, E., 2014. Arterial stiffness, the brain and cognition: a systematic review. Ageing Res. Rev. 15 (1), 16–27. http://doi.org/10.1016/j.arr.2014.02.002.

Taheri, S., Gasparovic, C., Huisa, B.N., Adair, J.C., Edmonds, E., Prestopnik, J., Rosenberg, G.A., 2011. Blood-brain barrier permeability abnormalities in vascular cognitive impairment. Stroke 42 (8), 2158–2163. http://doi.org/10.1161/STROKEAHA.110.611731.

Tofts, P., 2003. In: Tofts, P. (Ed.), Q Uantitative MRI of the Brain. John Wiley & Sons, London.

Tozer, D.J., Davies, G.R., Altmann, D.R., Miller, D.H., Tofts, P.S., 2005. Correlation of Apparent myelin measures obtained in multiple sclerosis patients and controls from magnetization transfer and multicompartmental T 2 analysis. Magn. Reson. Med. 53 (6), 1415–1422. https://doi.org/10.1002/mrm.20479.

Tukey, J.W., 1977. Exploratory Data Analysis. Addison-Wesley, pp. 43–44.

Turner, R., Oros-peusquens, A., Romanzetti, S., Zilles, K., Shah, N.J., 2008. Optimised in vivo visualisation of cortical structures in the human brain at 3 T using IR-TSE, 26, pp. 935–942. https://doi.org/10.1016/j.mri.2008.01.043.

Wahlund, L.O., Barkhof, F., Fazekas, F., Bronge, L., Augustin, M., Sjögren, M., Wallin, A., Ader, H., Leys, D., Pantoni, L., Pasquier, F., Erkinjuntti, T., Scheltens, P., 2001. A new rating scale for age-related white matter changes applicable to MRI and CT. Stroke 32 (6), 1318–1322. http://doi.org/10.1161/01.STR.32.6.1318.

Wardlaw, J.M., Smith, C., Dichgans, M., 2013a. Mechanisms of sporadic cerebral small vessel disease: insights from neuroimaging. Lancet Neurol. 12 (5), 483–497. http://doi.org/10.1016/S1474-4422(13)70060-7.

Wardlaw, J.M., Smith, E.E., Biessels, G.J., Cordonnier, C., Fazekas, F., Frayne, R., Dichgans, M., 2013b. Neuroimaging standards for research into small vessel disease and its contribution to ageing and neurodegeneration. Lancet Neurol. 12 (8), 822–838. http://doi.org/10.1016/S1474-4422(13)70124-8.

Wardlaw, J.M., Valdés Hernández, M.C., Muñoz-Maniega, S., 2015. What are white matter hyperintensities made of? Relevance to vascular cognitive impairment. J. Am. Heart Assoc. 4 (6), 001140. http://doi.org/10.1161/JAHA.114.001140.

Weller, R.O., Hawkes, C.A., Kalaria, R.N., Werring, D.J., Carare, R.O., 2015. White matter changes in dementia : role of impaired drainage of interstitial fluid, 25, pp. 63–78, 79. https://doi.org/10.1111/bpa.12218.

White, S.J., Hajnal, J.V., Young, I.R., Bydder, G.M., 1992. Use of fluid-attenuated inversion-recovery pulse sequences for imaging the spinal cord. Magn. Reson. Med. 28, 153–162. http://doi.org/10.1002/mrm.1910280116.

Wolff, S.D., Balaban, R.S., 1989. Magnetization transfer contrast (MTC) and tissue water proton relaxation in vivo. Magn. Reson. Med. 10, 135–144. https://doi.org/10.1002/mrm.1910100113.

Yarnykh, V.L., 2007. Actual flip-angle imaging in the pulsed steady state: a method for rapid three-dimensional mapping of the transmitted radiofrequency field. Magn. Reson. Med. 57 (1), 192–200. http://doi.org/10.1002/mrm.21120.